Supporting Information for:

A Long-lived Fe^{III}-(Hydroperoxo) Intermediate in the Active H200C Variant of Homoprotocatechuate 2,3-Dioxygenase: Characterization by Mössbauer, EPR, and DFT Methods

Katlyn K. Meier,[§] Melanie S. Rogers,[†] Elena G. Kovaleva,[#] Michael M. Mbughuni,[†]

Emile L. Bominaar,[§*] John D. Lipscomb,[†*] Eckard Münck[§*]

[§] Department of Chemistry, Carnegie Mellon University, Pittsburgh, Pennsylvania 15213, U.S.A.

[†]Department of Biochemistry, Molecular Biology and Biophysics and Center for Metals in Biocatalysis, University of Minnesota, Minneapolis, Minnesota 55455, U.S.A.

[#] Stanford Synchrotron Radiation Lightsource, 2575 Sand Hill Road, Menlo Park, CA 94025 U.S.A.

1. X-ray Crystallography Methods and Supplementary Results.

H200C was crystallized by the hanging-drop method at 20 °C in 13 – 15 % PEG6000, 0.1 M calcium chloride, 0.1 M MOPS, pH 7.0. Crystals were briefly transferred into a mother liquor solution containing 25% PEG400 as a cryoprotectant before cryo-cooling in liquid nitrogen and data collection at 100 K.

The anaerobic substrate complex was formed by first equilibrating all solutions and crystals of H200C in an anaerobic glove box for at least 18 h. Then a crystal was incubated with 2 mM anaerobic HPCA for 30 min, followed by brief transfer into a mother liquor containing 25% PEG400 as a cryoprotectant for cryo-cooling in liquid nitrogen inside the glovebox.

The XDS package[1] was used to process diffraction data. The 2,3-HPCD (PDB 3OJT) coordinates were used as an initial rigid body refinement model followed by cycles of restrained refinement with Refmac5[2], as part of the CCP4 program suite[3] and model building using Coot.[4] The 4 subunits of the single enzyme molecule present in the asymmetric unit were refined independently. Ligand refinement protocols were essentially the same as those described previously.[5,6] X-ray data processing and refinement statistics are summarized in Table S1. All structure figures were produced using PyMOL (The PyMOL Molecular Graphics System, Version 1.5.0.4 Schrödinger, LLC).

Table S1. X-ray data collection and refinement statistics for H200C 2,3-HPCD variant in free form and anaerobic complex with HPCA [a].

Dataset (PDB Code)	H200C (PDB 5BWG)	H200C-[HPCA] (PDB 5BWH)
Wavelength	0.9801 Å	0.9763 Å
Synchrotron (beamline)	Synchrotron Soleil (Proxima I)	DLS (I-03)
Spacegroup	$P2_12_12$	$P2_12_12$
Cell dimensions (Å)	110.7, 150.6, 96.3	110.4, 151.0, 96.5
Cell angles (deg)	90, 90, 90	90, 90, 90
Resolution range[a] (Å)	48.1 – 1.75 (1.84)	29.7 – 1.46 (1.54)
Reflections (observed/unique)	716646/160179	1025435/269165
R_{rim} [a, b] (%)	6.5 (78.5)	5.9 (71.0)
R_{pim} [a, c] (%)	3.4 (41.0)	3.4 (40.9)
Mean $\langle I\rangle/\sigma\langle I\rangle$ [a]	14.0 (1.9)	12.3 (2.0)
Completeness (%) [a]	98.9 (97.9)	96.9 (94.0)
R, R_{free}, test (%) [d]	14.5, 17.9, 5.0	12.2, 16.0, 5.0
RMSD [e] bond length (Å)	0.013	0.009
RMSD [e] angles (deg)	1.498	1.301
ESU [f] (Å)	0.073	0.041
Ramachandran Plot		
Allowed regions (%)	99.7	99.7
Additional regions (%)	0.3	0.3

[a] Values for the highest resolution shell are given in parentheses. [b] Redundancy-independent merging R factor: $R_{r.i.m} = \sum_{hkl}[N/(N-1)]^{1/2}\sum_i|I_i(hkl)-\langle I(hkl)\rangle| / \sum_{hkl}\sum_i I_i(hkl)$, where $\langle I(hkl)\rangle$ is the mean value of $I(hkl)$.[7] [c] Precision-indicating merging R factor: $R_{p.i.m} = \sum_{hkl}[1/(N-1)]^{1/2} \sum_i|I_i(hkl)-\langle I(hkl)\rangle| / \sum_{hkl}\sum_i I_i(hkl)$, where $\langle I(hkl)\rangle$ is the mean value of $I(hkl)$.[7] [d] $R = (\sum||F_{obs}|-k|F_{calc}||)/\sum|F_{obs}|$, where k is a scale factor. The R_{free} value was calculated with the indicated percentage of reflections not used in the refinement. [e] Root-mean-square deviation (RMSD) from ideal geometry in the final models. [f] Estimated overall coordinate error (ESU) based on maximum likelihood.

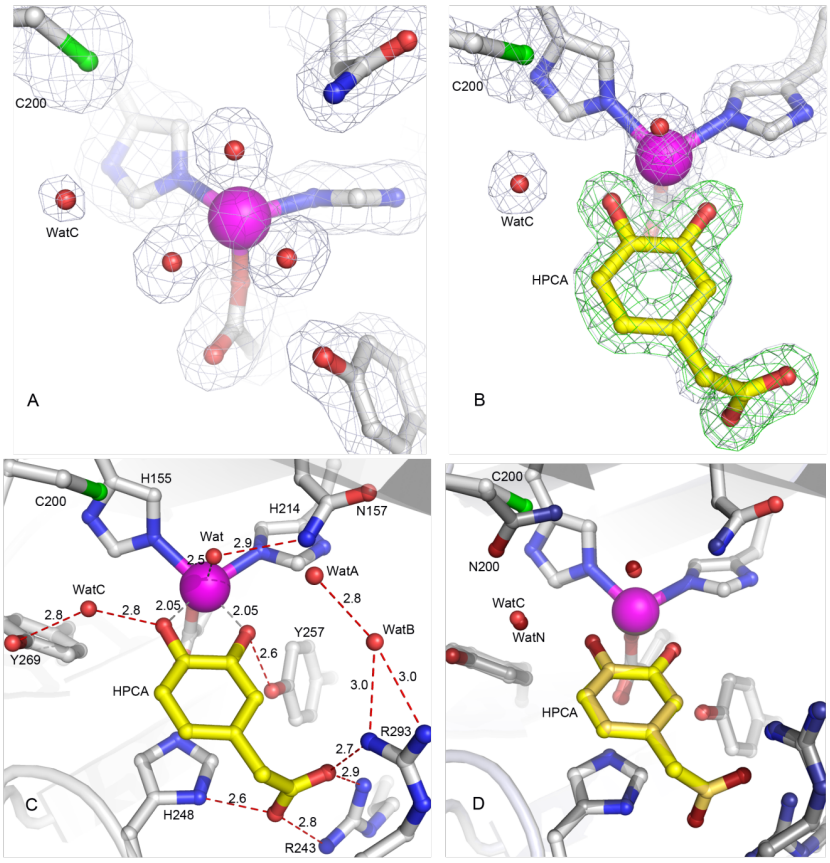

Figure S1. Active site environments in the H200C variant in resting state and in complex with HPCA. (A) H200C (PDB 5BWG), (B) H200C-HPCA complex (PDB 5BWH), (C) hydrogen-bonding interactions in the active site of H200C-HPCA complex (PDB 5BWH), (D) Overlay of active site structures of H200C (PDB 5BWH) and H200N variants (PDB 4Z6Q) in complex with HPCA. The blue $2F_{obs}–F_{calc}$ electron density map is contoured at 1.0 σ (A) and 1.5 σ (B). The green ligand-omit $F_{obs}–F_{calc}$ electron density map is contoured at 6.0 σ (B). Atom color code: gray, carbon (H200C); dark gray, carbon (H200N); yellow, carbon (HPCA, H200C); gold, carbon (HPCA, H200N); blue, nitrogen (H200C); dark blue, nitrogen (H200N); red, oxygen (H200C); dark red, oxygen (H200N); green, sulfur (H200C); purple, iron (H200C); bronze, iron (H200N). Red dashed lines show hydrogen-bonds (Å). Gray dashed lines indicate bonds or potential bonds to iron (Å). Cartoons depict secondary structure elements for H200C (gray) and H200N variants (light blue). WatA-C and WatN represent crystallographically observed (not metal-coordinated) solvent in the active site.

2. Discussion of the Mössbauer Spectra of Figures 3 and 4.

In this section we describe how the Mössbauer parameters listed in Table 1 were obtained. For convenience, the spectra of Figures 3 and 4 are shown here as Figures S2 and S3. Although the Mössbauer spectra depend on many parameters, one does not have to rely on multi-parameter fits because most of the critical unknowns can be isolated and determined with good precision by identifying the behavior of key features of the spectra under conditions of variable temperature and/or variable field.

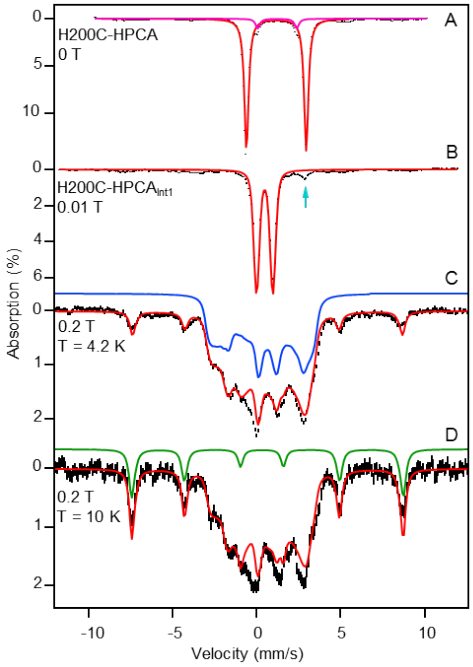

Figure S2. [Figure 3 of main text] (A) Zero-field, 4.2 K Mössbauer spectrum (black) of H200C-HPCA (simulation, red curve) and the minority species with ΔE_Q = 2.32 mm/s and δ = 1.20 mm/s (magenta curve). The spectra shown in panels A and B are raw data. Spectra shown in panels C and D were obtained by removing the high-spin ferric and high-spin ferrous impurities. (B, C) Spectra of the oxygenated intermediate, H200C-HPCA$_{Int1}$ = *Int1*, recorded at 4.2 K in parallel applied magnetic fields as indicated. (D) B = 0.2 T spectrum recorded at 10 K. The spectra in (C) and (D) contain a 6-line pattern (green curve) associated with the excited M_S = ±2 doublet of the S = 2 multiplet. The

absorption of this feature increases with increasing temperature, showing that $D > 0$. The dominant contributions of the central feature, blue in (C), are from the $M_S = 0$ and $M_S = \pm 1$ doublets.

At 4.2 K, the relaxation rate of the electronic spin was found to be slow compared to the nuclear precession frequencies. Consequently, the low temperature spectra of *Int1* are a superposition of five sub-spectra, one for each of the populated M_S levels of the $S = 2$ multiplet. The spectra of Figures S2C and D contain a 6-line pattern (green line in D) whose intensity increases as the temperature is raised from 4.2 K to 10 K. The behavior of this 6-line pattern suggests that it originates from molecules in the $M_S = \pm 2$ levels (NB: for $B = 0.2$ T both $M_S = \pm 2$ levels yield essentially the same spectrum). Since the $M_S = \pm 2$ levels are excited states, it follows that $D > 0$, as shown in the diagram of Figure S5. The intensity of this feature is determined by the Boltzmann factors that govern the population of the sublevels of the $S = 2$ state. From the experimentally determined intensities, we were able to extract the ZFS parameter, $D \approx +1.6$ cm^{-1} ($D_1 = (3/4)D = 1.2$ cm^{-1}).

Figure S2C shows that the central features of the Mössbauer spectra reflect to a large extent the $M_S = 0$ ground state that is mixed with the $M_S = \pm 1$ levels by the x and y components of the applied magnetic field. "Magnetization" curves, i.e. plots of $< \hat{S}_i >$ versus B, for the "$M_S = 0$" state are shown in Figure S5B. The magnetic splitting of the Mössbauer spectra is governed by the internal magnetic field $\mathbf{B}_{int} = -\langle\hat{\mathbf{S}}\rangle \cdot \mathbf{A}/g_n\beta_n$. The shapes of the magnetization curves depend mainly on D and E/D; $|\langle S_x\rangle| < |\langle S_y\rangle|$ for $E/D \neq 0$. Fitting the spectra for different applied fields requires $D = +1.6$ cm^{-1}, in good agreement with the value obtained from the Boltzmann populations at 4.2 K and 10 K. As shown in Figure 6 of the main text, we obtained the same

value for $D = (4/3)D_1$ by fitting the temperature dependence of the $g = 8.04$ parallel mode X-band EPR feature.

E/D can be determined in various ways. First, the intensity of the $g = 8.04$ EPR feature is proportional to $(\Delta_{-2})^2$, where (Δ_{-2}) refers to the splitting of the $M_S = \pm 2$ levels in zero field. $\Delta_{-2} = 3D(E/D)^2$ can be obtained from the EPR intensity which, with D known, is proportional to $(E/D)^4$. Therefore, a quantitative analysis of the EPR signal intensity using the known concentration of *Int1* provides a very sensitive measure of E/D. From this analysis we obtained $E/D = 0.055$.

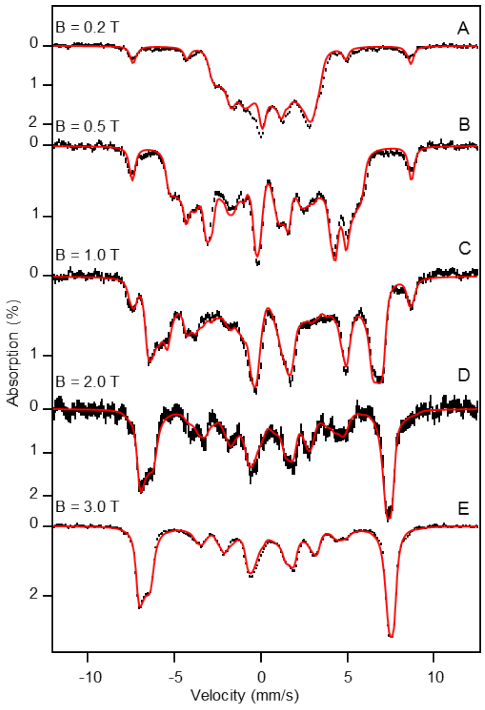

Figure S3. [Figure 4 of main text] 4.2 K Mössbauer spectra of *Int1* recorded in variable, parallel applied magnetic fields of (A) 0.2 T, (B) 0.5 T, (C) 1.0 T, (D) 2.0 T, and (E) 3.0 T. The black hash-mark curves are the spectra that result after subtraction of the minority Fe^{II} (6%) and Fe^{III} (8%) contaminants from the raw data. The Fe^{III} contaminant was simulated with parameters given in the caption of Figure S4. Red lines are spin Hamiltonian simulations generated using the parameters listed in Table 1 of the main text.

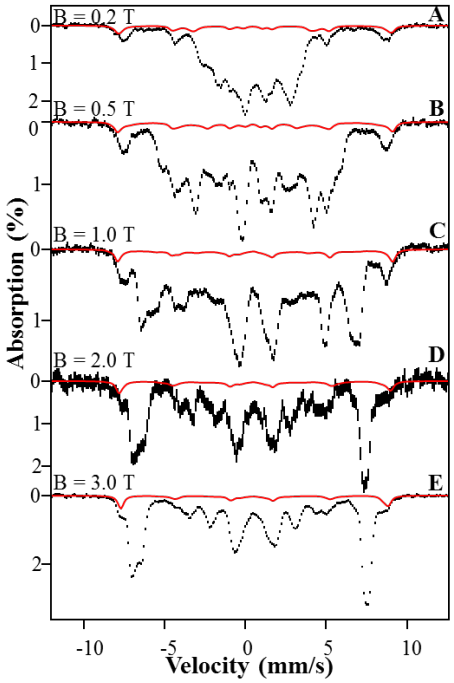

Figure S4. 4.2 K Mössbauer spectra of *Int1* recorded in variable, parallel applied magnetic fields of (A) 0.2 T, (B) 0.5 T, (C) 1.0 T, (D) 2.0 T, and (E) 3.0 T. The black hash-mark curves are the raw experimental spectra. The solid red curves represent the 8% high-spin ferric contaminant, and were generated using the parameters: D = -0.50 mm/s, E/D = 0.33 , ΔE_Q = 0.30 mm/s, η = 0, $A_0/g_n\beta_n$ = -21.9 T, δ = 0.45 mm/s.

Alternatively, E/D can also be obtained from the Mössbauer spectra. Given that the A_1-tensor for high-spin Fe^{III} is quite isotropic (for *Int1* within 2%), the anisotropy of $\mathbf{B}_{int}$ in the x-y plane is determined by E/D. Our EPR derived result was confirmed by analysis of the variable field Mössbauer spectra of Figures S2C and S3A-E which favor a value of $E/D < 0.08$. Moreover, the Mössbauer spectra establish that $E/D > 0.03$. The latter inequality follows from consideration of the magnetization behavior of the $M_S = \pm 1$ states which, together, are ≈ 48% populated at 4.2 K. For $E/D \leq 0.03$ the internal field associated with the $M_S = \pm 1$ states, $B_{int,z}(\pm 1)$, would rise steeply at low field, giving rise to a Mössbauer spectrum associated with the M_S = -1 level that would

contribute sharp features outside those associated with the M_S = 0 state, in contrast to the experimental observation.

Next we consider again the spectra associated with the M_S = ± 2 levels [green curve in Figure S2D]. For these two levels, <*S*> is such that $\langle S_z \rangle = \pm 2$, $\langle S_{x,y} \rangle \approx 0$ for $0 < B < 0.2$ T (recall that *z* is the unique axis). Hence, B_{int} is locked along the *z*-axis of the ZFS tensor for essentially all molecular orientations. This describes a situation for which B_{int} is fixed relative to the EFG tensor. In the principal axis frame *x*', *y*', *z*', with the largest EFG component along *z*', the EFG tensor is diagonal. We readily obtained the magnetic splitting $a_{1z}/g_n\beta_n = -21.6 \pm 0.1$ T, a_{1x} and a_{1y} of Table 1 were obtained from the 3.0 T spectrum using the known D_1 and $(E/D)_1$ values; $|\Delta E_Q| = (eQV_{zz}/2)(1+ \eta^2/3)^{1/2} = 0.97$ mm/s is known from the spectrum of Figure S2B. The experimental splitting of the 6-line pattern of Figure S2D requires a small positive component of the EFG along *z*. This can be achieved for positive as well as negative ΔE_Q. As discussed in the main text, knowledge of the orientation of the unique axis, *z*, in the EFG frame allows one to relate Mössbauer, EPR ^{17}O hyperfine structure and DFT results, and thus correlate spectroscopic information with a geometric structure. Determination of α and β turned out to be a rather arduous task (requiring a few hundred spectral simulations). With $B_{int,z}$ known, the line positions of the 6-line pattern depend on angles β and γ through the effective quadrupole interaction along the direction of B_{int}, namely $(eQV_{z'z'}/12)$ $(3\cos^2\beta - 1 + \eta\cos2\gamma \sin^2\beta)/2$ (there are small off-diagonal terms); because the electronic system is essentially uniaxial at $B = 0.2$ T the expression does not depend on α.

If the spin relaxation rate of *Int1* would be fast compared to the nuclear precession frequencies at 150 K, one could determine the sign of the quadrupole splitting from a high field spectrum

(although the Fe^{III} impurity would be bothersome). Unfortunately, this option is not available as *Int1* displayed broad and unresolved spectra at 150 K, indicating intermediate relaxation rates. Therefore, we have started our analysis with the B = 0.2 T spectra of Figures S2C and S2D, where the green curve indicates the contribution of the $M_S = \pm 2$ electronic doublet. The positions of the six lines of this doublet are reasonably well known (the two inner lines can be located after subtracting the approximate contribution of the M_S = 0 and ±1 levels). Analysis of the 6-line spectrum confines the polar angle β to the range 55° < β < 70°; the line positions are not sufficiently well known to determine β and $\eta\cos 2\gamma$ with accuracy as the effective component of the EFG along z is quite small. Next, we least-square fitted groups of four 4.2 K spectra which brings the magnetization behavior of the M_S = 0 and ± 1 levels into the problem (before attempting these fits we understood the origin of all lines in the spectra of Figures S2C and S3A-S3B. These fits converged to a solution for which the polar angles were $\alpha \approx$ 55-60° and $\beta \approx$ 70°. As shown in the main text, this result is significant as it locates the z-axis of the ZFS tensor in the (x', y', z') frame of the EFG tensor (the DFT studies revealed that the z'-axis is roughly along the direction defined by the O_{OOH}-Fe-O_{E267}) bond.

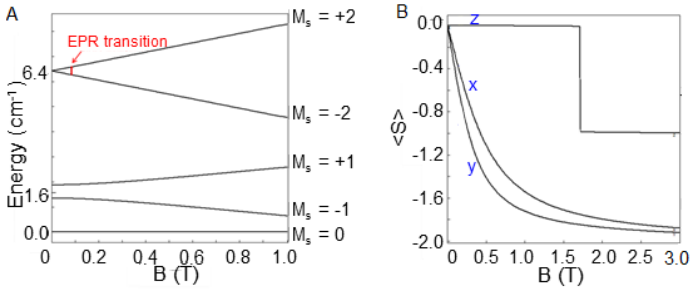

Figure S5. (A) Schematic energy levels of the S = 2 system. For simplicity the levels are labeled by M_S quantum numbers rather than by non-magnetic states ϕ^0, ϕ^{1s}, ϕ^{1a}, ϕ^{2s}, and ϕ^{2a}. For instance, $|\phi^{1s,1a}\rangle = (|M_S = +1\rangle \pm |M_S = -1\rangle)/\sqrt{2}$; see Hendrich and Debrunner.[8] (B) Spin expectation values for the *lowest* spin level of H200C-HPCA$_{Int1}$. $\langle \hat{S}_{x,y,z} \rangle$

are the expectation values of the electronic spin when B is applied along x, y, or z. The jump of $<\hat{S}_z>$ near B = 1.8 T is due to level crossing as the M_S = -1 state becomes the ground state for molecules for which B is along z.

The sensitivity of the data to α can be understood by inspection of Figure S5B which shows that, despite the small value of E/D, there is considerable anisotropy of $<S>$ in the x-y plane for B = 0.2 and 0.5 T. The solution with $\beta = 70°$ assures that the EFG frame is tilted such that the quadrupole interaction has a small positive component along z. The best fits to the experimental spectra were obtained for $\Delta E_Q < 0$, i.e. ΔE_Q = -0.97 mm/s. The asymmetry parameter η (= 0.55) was found to be quite soft, with acceptable fits for values of η approaching 1.0. In the limit η = 1, the EFG components are $V_{z'z'} = -V_{y'y'}$ and $V_{x'x'} = 0$, and the sign(ΔE_Q) depends on whether we choose the largest EFG component to be along z' or y'. Thus, our analysis admits a solution for $\Delta E_Q > 0$ provided $\eta \approx 1$.

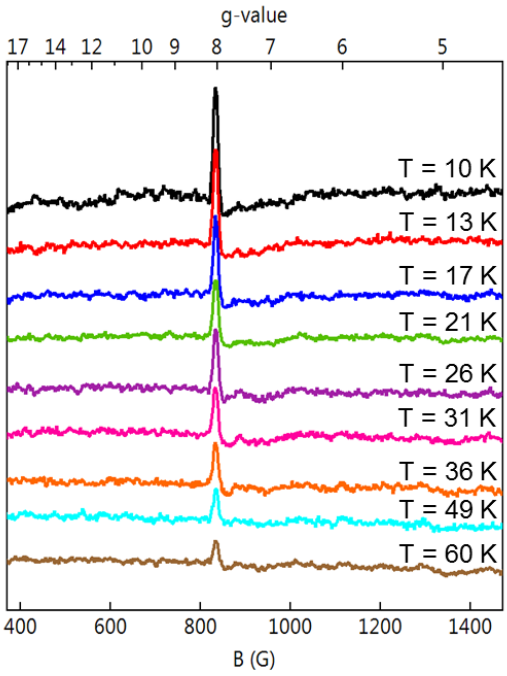

Figure S6. Parallel mode X-band EPR spectra of the g = 8.04 resonance of *Int1*. Spectra were collected for temperatures ranging from 10 K to 60 K. Conditions: 9.37 GHz frequency, 20 mW microwave power, 1 mT modulation. These data were used to generate the (signal ×T) analysis shown in Figure 6 of the main text.

3. Comments on ^{17}O Hyperfine Interactions.

In this section we discuss briefly how ^{17}O magnetic hyperfine interactions are handled when spin coupling is involved. There are two studies of superoxo radicals for which precise ^{17}O A-tensors have been reported. Chiesa et al.[9] studied an (η^2-O_2)/MgO system and determined $\mathbf{a}(^{17}O)$ = (-213, +20.2, +23.2) MHz, and Pietrzyk et al.[10] reported a comparable $\mathbf{a}(^{17}O)$ = (-166, +28.9, +29.4) MHz for an (η^2-O^2)/Ni ZSM-5 zeolite. In these two examples the large negative component of the a-tensor results from an unpaired electron in a $2p$ π_{xg} orbital for which the (negative) spin-dipolar contribution of the ^{17}O a-tensor is large along x; this component also has a negative contribution from the Fermi contact term. The quoted $\mathbf{a}(^{17}O)$ is the intrinsic magnetic hyperfine tensor in the S_R = ½, $\hat{\mathbf{S}}_R \cdot \mathbf{a}(^{17}O) \cdot \hat{\mathbf{I}}_O$ term, where S_R is the spin of the superoxo radical.

For the superoxo complex of H200N-4NC$_{Int1}$ we found a_{eff} (^{17}O) ≈ 180 MHz. Since the value of a_{eff} (^{17}O) is comparable to the largest component of the above cited superoxo radicals we may assume that that the largest component of the ^{17}O hyperfine tensor in H200N-4NC$_{Int1}$ is (approximately) along the unique axis, allowing us to use $a_{eff}(^{17}O) = a_z(^{17}O)$.[11] Owing to the antiferromagnetic exchange between the superoxo moiety and the Fe^{III}, the ^{17}O hyperfine interaction appears in the S = 2 representation as $A_z(^{17}O) = (-1/6)a_z(^{17}O)$, i.e. the interaction is scaled by the (-1/6) spin projection factor. The absence of observable ^{17}O broadening for *Int1* could be interpreted in two ways. Either H200C-HPCA$_{Int1}$ does not contain a superoxo radical (as suggested by our DFT results) or the easy axis, z, of *Int1* is essentially perpendicular to the direction of the largest component of $\mathbf{a}(^{17}O)$. [NB: Note that the zero-field splitting parameters of the H200N-4NC$_{Int1}$ superoxo complex and H200C-HPCA$_{Int1}$ have opposite signs (D_1 = -0.6 cm^{-1} vs +1.2 cm^{-1}). This suggests that the easy axes in the two complexes might be orthogonal].

On the other hand, if H200C-HPCA$_{Int1}$, like H200N-HPCA$_{Int1}$, were an Fe^{III}-OOH complex coupled to a substrate radical moiety, the experiment of Figure 5 would yield ^{17}O hyperfine splitting from the enriched peroxo ligand (with the radical on the HPCA substrate). This hyperfine structure would reflect covalent delocalization of α-spin density from the iron to the proximal oxygen, described by the transferred hyperfine term $\hat{\mathbf{S}}_1 \cdot \mathbf{a}(^{17}O) \cdot \hat{\mathbf{I}}_O$. When referring to the S = 2 state, this term is modified by the spin projection factor (+7/6) to give $\hat{\mathbf{S}} \cdot \mathbf{A}(^{17}O) \cdot \hat{\mathbf{I}}_O$, with $\mathbf{A}(^{17}O) = (+7/6)\mathbf{a}(^{17}O)$. We will elaborate on these considerations in section 4.7 after presenting the DFT analysis.

4. DFT Analysis of *Int1*.

A number of equi-electronic structures have been analyzed by DFT to determine their suitability as models of *Int1*. The models investigated include hydroperoxo and superoxo species in two substrate protonation states (i.e. protonated versus deprotonated). Among the OOH species, we have considered models, shown in Figure 7, in which either the proximal or distal oxygens are protonated.

4.1. Distal Hydroperoxo Models for *Int1*. Three computational models for *Int1* were studied (Models I, II, III of Figure 8). The models were derived from the crystal structure of the ES complex and consisted of the Fe and its facial triad (His155, His214, Glu267) with terminal atoms frozen, as well as the HPCA substrate and a hydroperoxo ligand. Also included were several second sphere residues whose positions were fixed as in the ES structure, and WatC of which the oxygen was fixed while the hydrogens were allowed to optimize freely to account for hydrogen bonding interactions with the substrate. In the following we refer to the various models as Model I, II, and III, which differ in the number of atoms included in the calculations (Figure 8). Model I includes Arg243, Arg293, Asn157 (with flexible NH_2 protons), Cys200, Trp192, His248, Tyr257, two additional crystallographic waters, and HPCA substrate. It is worth noting that in this model, the carboxylate group of HPCA is deprotonated and forms a salt bridge to one of the Arg residues. Two protonation states were considered for the coordinating oxygen atoms of the substrate, O_{C1} (closest to Cys200) and O_{C2} (hydrogen bonded to Tyr257); in one case both oxygens were deprotonated and in the other only O_{C1} was protonated. The DFT calculations and spin distribution analysis of Model I Fe^{III}–radical states revealed that the majority of unpaired spin density was delocalized out of the catechol ring with the radical predominantly located on

the salt-bridge-forming residue, Arg243. This finding raises serious concerns regarding effects on reactivity for this model. This discrepancy may be a consequence of an incomplete description of the second and third coordination spheres, i.e. due to the absence of hydrogen bonding partners in the vicinity of Arg243 that were not included in the calculation. To address this concern, Model II was considered.

Model II was constructed to force the spin density back onto the substrate by removing the two Arg residues (and two nearby waters) from Model I. The oxygen atoms of the carboxylate tail of the HPCA substrate were fixed from the geometry optimized structure of Model I to mimic the steric and electrostatic constraints of the salt bridge and second-to-third coordination sphere of the enzyme while removing the potential for extended delocalization of the spin density onto the arginines. Property calculations for Model II systems yielded solutions for which the spin density was predominantly localized on the oxygen atoms of the HPCA carboxylate tail rather than delocalized across the atoms of the substrate ring. Efforts to force the radical onto the substrate ring required a third model, Model III.

The primary difference between Models II and III is that the latter contained a truncated substrate, with the carboxylate tail replaced by a methyl group. Optimizations of the system of Model III had the added constraint that one of the hydrogen atoms of the methyl-modified HPCA tail was frozen in space to model the preferred orientation of the ring and tail based on calculations of Models I and II. Indeed, calculations for Model III resulted in a solution with substrate-radical character localized on the catechol ring and the iron coordinating atoms. We have analyzed key features of each model to distinguish between potential conformations of *Int1*. Of particular interest are the spin densities on the substrate O_{C1} and O_{C2} atoms, as they may give

rise to ^{17}O magnetic hyperfine broadening observable in parallel mode EPR spectra. The spin populations of the oxygen atoms in the broken symmetry calculations, as obtained in Models I and II, have the same (by definition positive) sign as the spin populations of the iron and belong to the spin system of the iron. In calculations of Model III, however, the oxygen atoms have a large negative spin density in the π lobes that are part of the substrate radical orbital while retaining some positive, albeit smaller, spin densities in the σ lobes. This latter observation is indicative of the mixed iron–radical origin of the spin densities at O_{C1} and O_{C2}, suggesting that a description of the magnetic hyperfine interactions of the ^{17}O nuclei requires a spin Hamiltonian that includes terms for the couplings of the $I(^{17}O)$ nuclear spin with the electronic spins of both the iron and the radical as discussed in section 3.

4.2 Energies, *J* Values, and Electric Hyperfine Parameters for Distal Hydroperoxo models. Tables S2-S4 list the DFT results obtained for Models I-III for the relative energies, exchange-coupling constants, and ^{57}Fe electric hyperfine parameters, respectively. For all Model–Protonation combinations, three conformations were identified with the axial hydroperoxo being hydrogen bonded to (a) O_{C1} in the first conformation, (b) O_{C2} in the second conformation, or (c) neither O_{C1} or O_{C2} in the third conformation (dihedral angle H-O-O-Fe ≈ 150°). The relative energies of the conformations are given in Table S2 for each protonation state.

Table S2. Relative energies for distal hydroperoxo conformations [a]

Substrate	Conformer	Model I	Model II	Model III
Deprot. [c]	OOH···O_{C1}	0	0/0 [b]	0
	OOH···O_{C2}	2737	2792/1329 [b]	2593
	OOH	2819	2537/502 [b]	1169
Prot. [d]	OOH···O_{C1}	678	1108	1501
	OOH···O_{C2}	2198	2415	2275
	OOH	0	0	0

[a] Relative energies of broken symmetry states in wavenumbers using B3LYP/6-311G.

[b] Italics: results obtained with TZVP for 6-311G optimized structure.

[c] O_{C1} and O_{C2} of substrate are deprotonated.

[d] O_{C1} is protonated, O_{C2} is deprotonated.

Table S2 shows that one conformation is consistently lowest in energy for all three models. The lowest conformations are OOH···O_{C1} and OOH for the deprotonated and protonated substrates, respectively (first and sixth row). On this criterion alone, these conformers appear to be the best candidates for *Int1*. However, both energy order and energies of the higher-lying conformations display a significant dependence on the model. As an example, the middle column (Model II) of Table S2 shows the results obtained with a basis set that includes polarization functions, TZVP. These calculations resulted in lower excitation energies for both excited conformations (Model II, upper half). In addition to the basis set dependence, there is the distinct possibility that the hydroperoxo-H in the OOH conformation is engaged in interactions with parts of the structure not considered in our models. Given these uncertainties, it seems prudent at

this juncture not to dismiss any of the conformations at higher energy as potential formulations of *Int1*. In particular, the OOH conformation for Model II presents a plausible alternative.

4.3 Comparison of Exchange-Coupling Constants. The ligands of paramagnetic transition-metal ions are known to acquire spin density by covalent delocalization of the ligand electrons into the metal 3d orbitals. In the case of the metal–ligand interactions of a high-spin Fe^{III}, which has a half-filled 3d shell containing five spin-up electrons, the spin polarization of a ligand can only be due to the transfer of spin-down density into the vacant spin-down orbitals of the metal. This transfer would then lead to a ligand spin density with the same sign as that of the metal; transfer of spin-up density is obviously forbidden as the spin-up orbitals of high-spin Fe^{III} are occupied. Thus, if a spin-down electron is removed from a ligand orbital to obtain a ligand radical that is ferromagnetically coupled to the metal spin, this orbital will no longer contribute to the ligand-to-metal transfer. Alternatively, if a spin-up electron is removed to obtain an antiferromagnetic (actually, a broken symmetry) state, the transfer is still allowed. As transfer lowers energy, the energy of the antiferromagnetic state becomes lower than the energy of the ferromagnetic state, effectively leading to an antiferromagnetic coupling of the ligand and metal spins that is expressed by $J > 0$ in the convention $J\hat{\mathbf{S}}_1 \bullet \hat{\mathbf{S}}_2$. This narrative provides a simple explanation for the trends in the J values listed in Table S3.

Addition of a positive charge, perhaps by protonation of the substrate, suppresses delocalization away from the substrate and consistently results in small and/or ferromagnetic J values (lower half of Table S3). Despite providing weaker sequestration of electron density than covalent O-H bonds (lower half of Table S3), hydrogen bonds formed between the hydroperoxo and the coordinating oxygen atoms of the substrate (listed in the first two rows of Table S3) lead

to *J* values that are smaller than those obtained when these hydrogen bonds are absent (third row). The entries of Table S3 show that this reasoning holds for all three models. Our calculations suggest that antiferromagnetic coupling is further enhanced by removal of crystallographic WatC and its hydrogen bonding interaction with O_{C1} (see *J* value in parentheses in Table S3).

Table S3. Exchange-coupling constants, *J*, for distal hydroperoxo conformations [a]

Substrate	Conformer	Model I	Model II	Model III
Deprot. [d]	OOH···O_{C1}	2.3	13.4/18.1 [c]	4.3
	OOH···O_{C2}	32.6	63.5/78.4 [c]	12.9
	OOH	103.6 (175.4)[b]	147.0/174.7 [c]	167.6
Prot. [e]	OOH···O_{C1}	–0.5	–2.8	–16.0[f]
	OOH···O_{C2}	–0.8	–2.5	–4.9[f]
	OOH	–0.7	–2.8	–124.8

[a] *J* in wavenumbers in $J\widehat{\boldsymbol{S}}_{\boldsymbol{1}} \bullet \widehat{\boldsymbol{S}}_{\boldsymbol{2}}$ convention evaluated from the vertical $S = 3$ excitation energy at the optimized BS structure obtained with B3LYP/6-311g.

[b] Without WatC.

[c] Second number obtained with B3LYP/TZVP.

[d] O_{C1} and O_{C2} of substrate are deprotonated.

[e] O_{C1} is protonated, O_{C2} is deprotonated.

[f] Solutions with large spin densities on His248.

Similarly, the presence of the salt bridge in Model I explains the smaller calculated *J* values as compared to those calculated for Model II (see rows 1-3). Furthermore, the observation that the calculated *J* values for Model III are smaller than those of Model II (first and second rows of Table S3) is readily explained by considering the electron donating capacity of the deprotonated substrate radical which is weaker for a monoanionic radical (Model III) than for a dianionic

radical (Models I/II). The third row appears to be a marginal exception, and required a more detailed analysis. The OOH···O_{C1} conformation yielded consistently lower J values than the OOH···O_{C2} conformation (compare first and second rows of Table S3), which suggests that the hydrogen bond between the hydroperoxo and O_{C1} has a larger effect on the redox active orbital of the substrate than a hydrogen bond to O_{C2}. The explanations presented here focus on the antiferromagnetic term J_{AF} in the expression $J = J_F + J_{AF}$, as well as the effects of protonation and hydrogen bonding on the denominator, U, in the second-order expression $J_{AF} \sim \langle h \rangle^2/U$. The J_F term appears to be particularly prominent in the last row for Model III and is likely due to the spin delocalization of the substrate and metal into orthogonal p-orbitals of the coordinating O atoms.

The experimental lower bound, $J > 40$ cm^{-1}, clearly excludes the structures listed in the lower half of Table S3 as formulations of *Int1*. *Therefore, if Int1 were a distal hydroperoxo species, the substrate must be deprotonated*. Among the conformations in the upper half of Table S3, only those in the second and third rows appear to be admissible as candidates for *Int1*. This finding, along with the energy analysis that suggests the third row is energetically favored over the second in Table S2, is consistent with a conformation for *Int1* that is closest to the OOH conformer.

4.4 Comparison of ^{57}Fe Hyperfine Coupling Constants. Table S4 lists the ^{57}Fe electric hyperfine parameters for the six distally protonated hydroperoxo models. The isomer shifts listed in the table are typical for high spin Fe^{III} and are all in good agreement with experiment. Therefore, with differences in the calculated δ values being so small, it is not possible to select or exclude potential models of *Int1* on this property alone. However, the quadrupole splittings in

Table S4 appear to be more discerning than the isomer shifts, with the values in the lower half of the table being consistently larger than the experimental value for $|\Delta E_Q|$ (0.97 mm/s). This observation further corroborates the conclusion drawn from analysis of the *J* values, namely that the substrate bound in *Int1* must be deprotonated. The ΔE_Q values in the second and third rows of Table S4 show a satisfactory agreement with the experimental value, especially for Models I and II. For Model II, Table S4 also lists ΔE_Q and η values obtained with the basis set TZVP that includes polarization functions. The dependence of these parameters on the choice of basis set appears to be rather small.

Table S4. ^{57}Fe electric hyperfine parameters from DFT for distal hydroperoxo conformations [a]

Substrate	Conformer	Model I			Model II			Model III		
		δ	ΔE_Q	η	δ	ΔE_Q	η	δ	ΔE_Q	η
Deprot [c]	$OOH\cdots O_{C1}$	0.53	1.075	0.358	0.53	1.117 1.064[b]	0.379 0.567[b]	0.51	–1.487	0.906
	$OOH\cdots O_{C2}$	0.54	0.801	0.872	0.54	–0.831 –0.826[b]	0.977 0.741[b]	0.51	–1.249	0.236
	OOH	0.54	0.854	0.809	0.55	0.873 –0.866[b]	0.811 0.929[b]	0.51	–1.126	0.284
Prot [d]	$OOH\cdots O_{C1}$	0.50	1.548	0.168	0.49	1.532	0.288	0.48	1.536	0.592
	$OOH\cdots O_{C2}$	0.51	1.699	0.896	0.50	–1.713	0.919	0.49	–1.756	0.699
	OOH	0.51	1.359	0.134	0.50	1.347	0.061	0.49	1.418	0.674

[a] δ and ΔE_Q in mm/s; obtained for the BS state with B3LYP/6-311G.

[b] Values obtained with basis TZVP by single point calculations for the 6-311G optimized geometry in the BS state.

[c] O_{C1} and O_{C2} of substrate are deprotonated.

[d] O_{C1} is protonated, O_{C2} is deprotonated.

The ΔE_Q and η values of Table S4 are quoted in a 'proper' coordinate frame for which $V_{z'z'}$ is along the largest component of the EFG. Use of a proper coordinate frame can be quite misleading for large η values ($\eta \approx 1$) in the limit ($V_{zz} \approx -V_{yy}$), where subtle changes render either the negative ($\Delta E_Q < 0$) or positive ($\Delta E_Q > 0$) component largest in magnitude. For example, in Table S4, row 3, Model II the sign of ΔE_Q changes from positive to negative upon switching to the TZVP basis set. In either case, *as in all cases of Table S4*, the large negative component of the EFG is roughly along the O-Fe-O_{E267} direction. Comparing the values (TZVP in italics) for $eQV_{xx}/2$; $eQV_{yy}/2$; $eQV_{zz}/2$ = {*+0.024*, -0.075; *+0.649*, +0.790; *-0.672*, -0.716} shows that the differences in the individual components are rather small. In this limit, a change in the sign of ΔE_Q can be brought about by minor changes in the principal values of the EFG that render either the positive or negative component to be largest in magnitude.

We have investigated models for which the proton of the hydroperoxo moiety resides on the proximal oxygen, but have not found a solution that fits to *Int1*.

4.5 Proximal Hydroperoxo Models for *Int1*. Calculations for the proximally protonated hydroperoxo species were performed for Model I with the proton now on the proximal oxygen. The geometry optimizations converged to one conformation with a dihedral angle H-O-O-Fe ≈ 140°. The results for the ^{57}Fe electric hyperfine parameters (which are quite independent of the model used) and the exchange-coupling constant, J, between the substrate radical and the high-spin Fe^{III} are listed in Table S5 for both the deprotonated substrate ($HPCA^{3-}$) and the O_{C1}-protonated form. The protonated substrate form has a small ferromagnetic J, similar to the distally protonated hydroperoxo conformer. This observation leaves only the deprotonated substrate form, which has admissible J and ΔE_Q values, as a viable candidate for *Int1*. However,

the value $\delta = 0.60$ mm/s for the deprotonated species appreciably exceeds the experimental value for the isomer shift (0.48 mm/s). Together, the large value for the relative energy and the 0.12 mm/s difference in calculated versus experimental isomer shifts suggest that *Int1* is not a proximally protonated hydroperoxo species.

Table S5. Parameters from DFT for proximal hydroperoxo species.[a]

Substrate	δ (mm/s)	ΔE_Q (mm/s)	η	J [b] (cm^{-1})	E [c] (cm^{-1})
Deprot.	0.60	0.894	0.731	65.5	5199
Prot.	0.58	1.644	0.319	−1.1	3863

[a] δ and ΔE_Q in mm/s; obtained for the BS state with B3LYP/6-311G.

[b] J in $J\hat{\mathbf{S}}_1 \bullet \hat{\mathbf{S}}_2$ convention evaluated from the vertical $S = 3$ excitation energy at the optimized BS structure obtained with B3LYP/6-311G.

[c] Energy relative to the energy of the corresponding lowest deprotonated/protonated substrate conformation for Model I in Table S2.

4.6 Superoxo Models for *Int1*. Our experimental data do not rule out the possibility that *Int1* is a superoxo complex as the unique axis, *z*, could be along a minor component of $\mathbf{A}(^{17}O)_{superoxo}$. DFT calculations for the superoxo species were performed for a model similar to Model I, but with an O_2 moiety instead of a hydroperoxo functional group at the position *trans* to E267. The results for the ^{57}Fe electric hyperfine parameters and the exchange-coupling constant, *J*, between the superoxo radical and the high-spin Fe^{III} are listed in Table S6 for both the deprotonated substrate ($HPCA^{3-}$) and the O_{C1}-protonated forms.

The calculations resulted in an unpaired electron of the superoxo moiety in the out-of-plane (Fe-O-O) orbital π^*_{out}, and the electron reducing O_2 to $O_2^{\bullet-}$ in the doubly occupied in-plane

orbital π^*_{in}. This electronic configuration provides a favorable condition for overlap of the L–M resonance of the spin-down π^*_{in} electron in the ferromagnetic state, which leads to a strong ferromagnetic coupling between the iron and the superoxo radical (fourth column of Table S6). The strongly favored $S = 3$ ground state for the superoxo model predicted by the calculations disagrees with the $S = 2$ ground state observed for *Int1*.

Table S6. Parameters from DFT for superoxo species [a]

Substrate	δ (mm/s)	ΔE_Q (mm/s)	η	J [b] (cm^{-1})	E (cm^{-1})
Deprot.	0.63	−1.338	0.711	−158.2	–
Prot.	0.70	2.022	0.731	−131.5	7068 [c]

[a] δ and ΔE_Q obtained for the BS state with B3LYP/6-311G.

[b] J in $J\hat{\mathbf{S}}_1 \bullet \hat{\mathbf{S}}_2$ convention evaluated from the vertical $S = 3$ excitation energy at the optimized BS structure obtained with B3LYP/6-311g.

[c] Energy relative to the energy of the corresponding lowest deprotonated substrate conformation for Model I in Table S2.

If a ferromagnetic superoxo state can be trapped for the H200C variant one would look for a parallel mode EPR feature characteristic of an $S = 3$ system. Possible signals might arise from the $M_S = \pm 3$ non-Kramers doublet near $g = 12$ (provided E/D is not too small as the signal intensity is proportional to $(E/D)^6$) or the $M_S = \pm 2$ doublet near $g = 8$. However, this state would most profitably be explored by Mössbauer spectroscopy.

4.7 Evaluation of ^{17}O Hyperfine Interactions: **Covalent Delocalization and Radical Contribution in Exchange Coupled Systems.** We have prepared *Int1* samples for EPR analysis where the introduced O_2 was enriched with ^{17}O. As argued above, the enriched oxygen would reside in the hydroperoxo ligand, with the radical on the HPCA substrate. In principle, we could

also have enriched either the oxygen of O_{C1} or O_{C2} of the substrate. (This non-trivial procedure is beyond the scope of the present work.) In this case the enriched oxygens would be exposed to the spin systems of both the iron and the substrate semiquinone radical, leading to a ^{17}O hyperfine tensor that has two contributions: one originating from the covalent delocalization of α spin density of the Fe^{III} onto these oxygens and another from the radical. In the following we briefly describe how both contributions have been obtained from DFT.

The magnetic hyperfine interactions of the ^{17}O nuclei of oxygen atoms that are part of a ligand radical (R, e.g. superoxo or a HPCA$^{\bullet}$) are described by the Hamiltonian

$$\widehat{\mathcal{H}}_{\mathrm{hf}} = \hat{\mathbf{I}}_{\mathrm{O}} \cdot \left(\mathbf{a}_{\mathrm{R}} \cdot \hat{\mathbf{S}}_{\mathrm{R}} + \mathbf{a}_1 \cdot \hat{\mathbf{S}}_1\right) \qquad \text{(S1)}$$

The first term, involving the radical spin $S_R = ½$, represents the coupling of the unpaired radical electron to the ^{17}O nucleus. The second term describes the interaction of the ^{17}O nucleus with spin density induced by the iron onto the oxygen. If only the Fermi contact interaction is considered, the coupling tensors, a_R and a_1, are isotropic and the internal magnetic field at the ^{17}O nucleus can be expressed as

$$g_{\mathrm{n}}\beta_{\mathrm{n}}B_{\mathrm{int}}^{\mathrm{F}} = (a_{\mathrm{R}} + 5a_1)/2 \qquad \text{(S2)}$$

in the ferromagnetically (F) coupled state ($S = 3$, spins of radical and iron are parallel) and as

$$g_{\mathrm{n}}\beta_{\mathrm{n}}B_{\mathrm{int}}^{\mathrm{BS}} = (-a_{\mathrm{R}} + 5a_1)/2 \qquad \text{(S3)}$$

in the broken symmetry state (BS) in which the radical spin has been flipped. Substituting for $B_{\mathrm{int}}^{\mathrm{F}}$ and $B_{\mathrm{int}}^{\mathrm{BS}}$ the DFT values for the Fermi contact field in the two states yields two equations from which the DFT values for a_{R} and a_1 have been solved. In an analogous manner one can extract the spin-dipolar (SD) tensors $\mathbf{a}_{\mathrm{R}}^{\mathrm{SD}}$ and $\mathbf{a}_1^{\mathrm{SD}}$ provided the principal axes of the SD tensors obtained for the two states are collinear, an assumption supported by the DFT calculations of the systems considered here. From this analysis one obtains the calculated ^{17}O magnetic hyperfine

tensors in the uncoupled representations $\hat{\mathbf{S}}_1 \cdot \mathbf{a}_1 \cdot \hat{\mathbf{I}}_O$ and $\hat{\mathbf{S}}_R \cdot \mathbf{a}_R \cdot \hat{\mathbf{I}}_O$. Since the data were analyzed using the $S = 2$ Hamiltonian of the coupled system, we have to multiply the local tensors with the appropriate spin projection factors to obtain $\hat{\mathbf{S}} \cdot \mathbf{A}(^{17}O) \cdot \hat{\mathbf{I}}_O$ where

$$\mathbf{A}(^{17}O) = -(1/6)\mathbf{a}_R + (7/6)\mathbf{a}_1 \quad \text{(S4)}$$

In the main text we have presented a plot of A_{eff} (defined in eq 5) for Model III. Figure S7 shows the equivalent plots for Models I and II. As pointed out in the main text, the main amplitude of the radical resides on Arg243 in Model I (Figure 8) and on the oxygens of the carboxylate tail of the substrate in Model II. Comparison of the plots for Models I, II and III (Figures 10 and S7) shows that the magnitude of A_{eff} for O_{C1} and O_{C2} shows little dependence on the location of the radical, suggesting that the values of A_{eff} are dominated by covalent delocalization (second term in eq S1). For the $S = 2$ multiplet the iron contribution has the spin projection factor +7/6 whereas the contribution of the radical at O_{C1} and O_{C2} is suppressed by the much smaller factor (-1/6) according to eq S4.

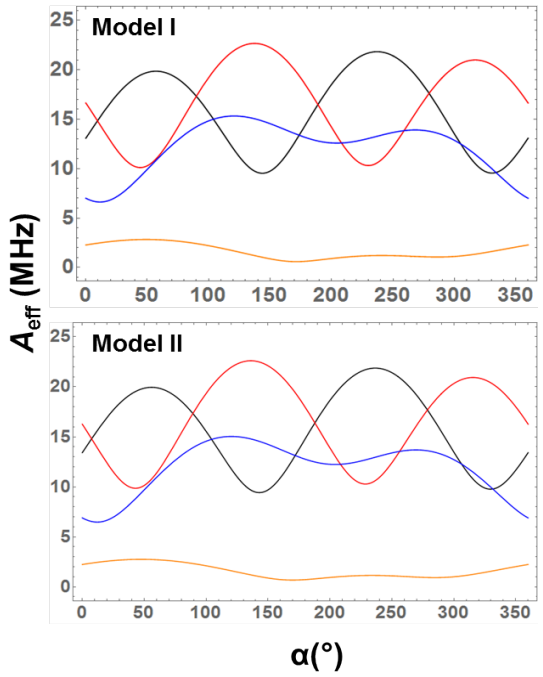

Figure S7. Plot of A_{eff} calculated for O_{C1} (red curves) and O_{C2} (black curves) of the HPCA substrate, and O_{prox} (blue) and O_{dist} (orange) of the hydroperoxo ligand. The plots were prepared using $\beta = 70°$.

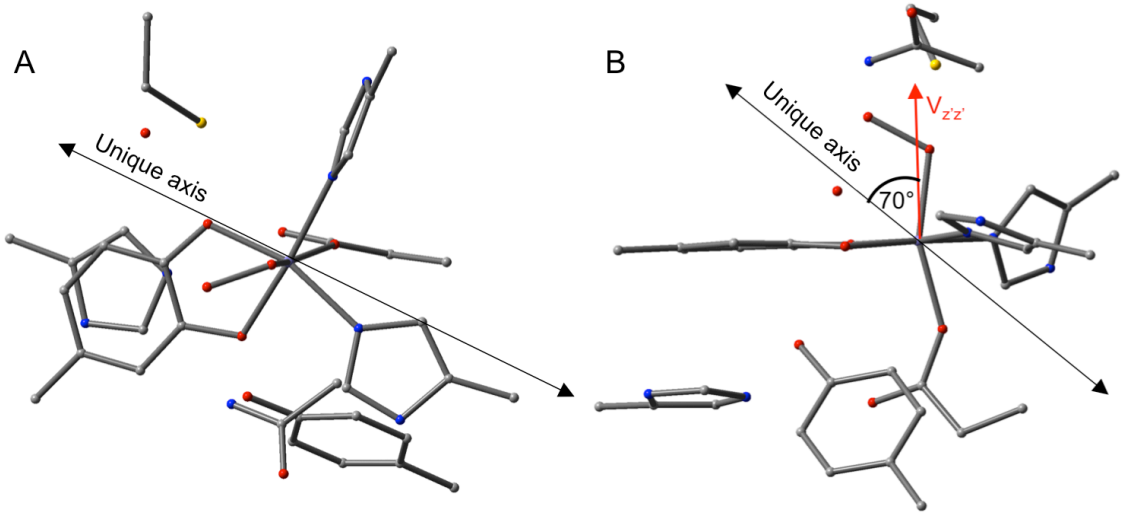

Figure S8. Orientation of the unique axis (the z axis of the ZFS tensor) relative to the molecular structure. (A) View approximately along the major component of the EFG tensor, $V_{z'z'}$. (B) View in the plane of the aromatic ring of the substrate. As implied by Figure 10, the unique axis is nearly parallel to the smallest component of the ^{17}O A-tensor of the proximal O of the hydroperoxo ligand.

4.8 Analysis of the Proton Coupled Electron Transfer Process

Figure S9 shows the results of the intrinsic reaction coordinate (IRC) calculations of the PCET process. Figure S9A presents the correlation between the distances of the transferring proton to the donor and acceptor atoms, O_D and O_A, along the IRC. The plot exhibits the typical hyperbolic shape where the increase of the $O_D\cdots H$ distance is correlated with a shortening of the $H\cdots O_A$ distance. Figure S9B displays the system energy along the correlation path of Figure S9A, using as coordinate, *x*, the normalized distance traversed by the proton along the curved path. As mentioned above, the TS lies about 800 cm^{-1} above the initial state of the process. After reaching the TS, the energy curve steeply decays to reach the final state. To obtain a better understanding of this behavior, Figure S9C shows the energy along the IRC plotted as a function of the O-H bond "breaking and making" coordinate, *y*, which is a measure of the $O_D\cdots H$ distance before the TS and of the $H\cdots O_A$ distance after the TS. More precisely, the coordinate *y* has been defined as

$$y = \frac{(O_D\cdots H) - (O_D{-}H)_{init}}{(O_D\cdots H)_{TS} - (O_D{-}H)_{init} + (H\cdots O_A)_{TS} - (H{-}O_A)_{fin}} \qquad \text{(S5a)}$$

before the TS and as

$$y = \frac{(O_D\cdots H)_{TS} - (O_D{-}H)_{init} + (H\cdots O_A)_{TS} - (H\cdots O_A)}{(O_D\cdots H)_{TS} - (O_D{-}H)_{init} + (H\cdots O_A)_{TS} - (H{-}O_A)_{fin}} \qquad \text{(S5b)}$$

after the TS; the denominators were introduced to normalize y to the range [0, 1]. This coordinate has been illustrated by dotted lines in Figure S9A. The energy is confined to a narrow range for $y < 0.9$ (see Figure S9C). At $y = 0.9$, where 90% of the bond breaking and making has been accomplished, the energy is approximately equal to the initial energy. Thus, 90% of the bond breaking and making takes place in an energy range of about 800 cm^{-1}. The black dots in

Figure S9C mark (a) the point where the spin populations of the substrate and O_2 moiety are equal (labeled "cross 1") and (b) the point where the populations of the transfer orbital at the substrate and the O_2 moiety are equal (labeled "cross 2"). As expected from the nature of the ET process, the two points nearly coincide. Cross 2 can be interpreted as the point where the electron donor and acceptor levels cross; the contour of the transfer orbital (down-spin-HOMO – 1) at this crossing point is shown in Figure 12B. The level crossing is located after the TS state of the overall PCET process, confirming that the ET process lags the PT (see main text). The energy drop for $y > 0.9$ may reflect the transformation of the system from a rather strained S_{ox3} conformation to a more relaxed hydroperoxo conformation as well as energy contributions associated with the completion of the ET process.

Since WatC continues to act as a HB donor to O_{Cl} during the PCET and the transferring proton remains hydrogen bonded, initially to O_A and finally to O_D, the number of hydrogen bonds appears to be conserved in the process. However, the number of HBs increases by one in passing from the lowest superoxo conformation S_{ox1} to the highest one, S_{ox3}, due to the conversion of WatC from HB acceptor to HB donor. As the catalytic cycle is likely to pass through the lowest superoxo conformation, WatC is expected to be one of the factors responsible for determining the kinetics and thermodynamics of the reaction. Furthermore, if WatC were absent, the middle S_{ox2} conformation would assume the role of lowest superoxo conformation. In that case, the barrier to reach the reactive superoxo conformation, S_{ox3}, would likely increase dramatically, suggesting that WatC plays an essential role in the reaction mechanism of the H200C variant.

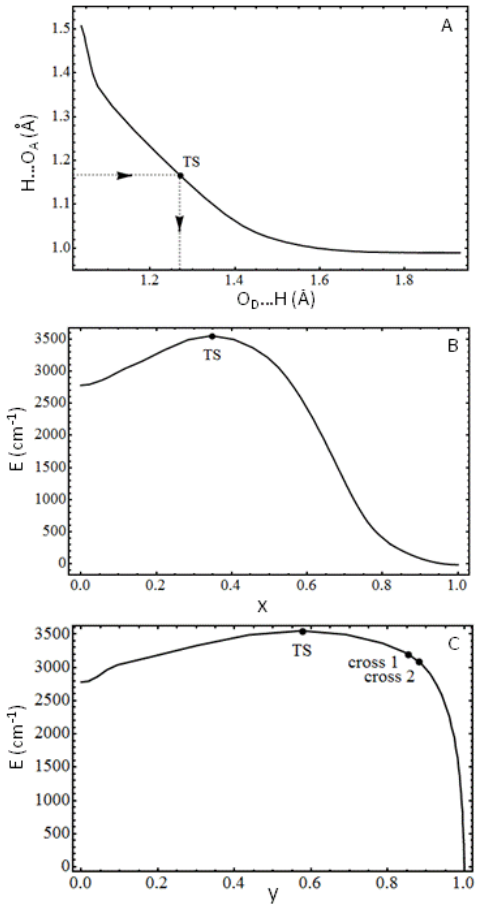

Figure S9. (A) Plot displaying the correlation between the distances of the transferring proton to the donor and acceptor atoms, O_D and O_A, along the IRC of the PCET. (B) Plot of the system energy along the correlation path of (A), using as coordinate, *x*, the normalized distance traversed by the proton along the curved path. (C) Energy curve along the IRC plotted as a function of the O-H bond "breaking and making" coordinate *y*.

REFERENCES

(1) Kabsch, W. *XDS, Acta Crystallogr., Sect. D: Biol. Crystallogr.* **2010**, *66*, 125-132.

(2) Murshudov, G. N.; Skubak, P.; Lebedev, A. A.; Pannu, N. S.; Steiner, R. A.; Nicholls, R. A.; Winn, M. D.; Longa, F.; Vagin, A. *Acta Crystallogr., Sect. D: Biol. Crystallogr.* **2011**, *67*, 355-367.

(3) Winn, M. D.; Ballard, C. C.; Cowtan, K. D.; Dodson, E. J.; Emsley, P.; Evans, P. R. *Acta Crystallogr D* **2011**, *67*, 235-242.

(4) Emsley, P.; Cowtan, K. *Acta Crystallogr.* **2004**, *E60*, 2126-2132.

(5) Kovaleva, E. G.; Lipscomb, J. D. *Science* **2007**, *316*, 453-457.

(6) Kovaleva, E. G.; Lipscomb, J. D. *Biochemistry* **2012**, *51*, 8755-8763.

(7) Weiss, M. S. *J. Appl. Cryst.* **2001,** *34*, 130-135.

(8) Hendrich, M. P.; Debrunner, P. G. *BioPhys. J.* **1989**, *56,* 490-506.

(9) Chiesa, M.; Giamello, E.; Paganini, M. C. *J. Chem. Phys.* **2002**, *116,* 4266-4274.

(10) Pietrzyk, P.; Podolska, K.; Mazur, T.; Sojka, Z. *J. Am. Chem. Soc.* **2011**, *133,* 19931-19943.

(11) Mbughuni, M. M.; Chakrabarti, M.; Hayden, J. A.; Bominaar, E. L.; Hendrich, M. P.; Münck, E.; Lipscomb, J. D., *Proc. Natl. Acad. Sci. U. S. A.* **2010,** *107*, 16788-16793.